Dynamic Characterization of the Water Binding Loop in the P-Type Cardiotoxin: Implication for the Role of the Bound Water Molecule†

Shih-Che Sue,‡ Harold C. Jarrell,§ Jean-Robert Brisson,§ and Wen-guey Wu*,‡

Department of Life Sciences, National Tsing Hua University, Hsinchu 30043, Taiwan, and Institute for Biological Sciences, National Research Council, Ottawa K1A 0R6, Canada

Received April 25, 2001; Revised Manuscript Received August 27, 2001

ABSTRACT: Recent studies of cobra P-type cardiotoxins (CTXs) have shown that the water-binding loop (loop II) plays a crucial role in toxin binding to biological membranes and in their cytotoxicity. To understand the role of bound water in the loop, the structure and dynamics of the major P-type CTX from Taiwan cobra, CTX A3, were determined by a comprehensive NMR analysis involving ^{1}H NOESY/ROESY, ^{13}C{^{1}H} NOE/T_1 relaxation, and ^{17}O triple-quantum filtered NMR. A single water molecule was found to be tightly hydrogen bonded to the NH of Met26 with a correlation time (5−7 ns) approaching the isotropic tumbling time (3.8−4.5 ns) of the CTX A3 molecule. Surprisingly, despite the relatively long residence time (ca. 5 ns to 100 μs), the bound water molecule of CTX A3 is located within a dynamic (order parameter $S^2 \sim 0.7$) and solvent accessible loop. Comparison among several P-type CTXs suggests that proline residues in the consensus sequence of MxAxPxVPV should play an important role in the formation of the water binding loop. It is proposed that the exchange rate of the bound water may play a role in regulating the lipid binding mode of amphiphilic CTX molecules near membrane surfaces.

Cobra venom consists of a wide diversity of cardiotoxins (or cytotoxins, CTXs)[1] with amino acid variation located mainly near the tip of loop I and loop II of their three-fingered β-sheet structure (*1*, *2*). Two distinct types of CTXs, i.e., P- and S-type, can be distinguished by the presence of Pro31 and Ser29, respectively, near the tip of loop II (*3*). P-Type CTXs bind more strongly to neutral phospholipid bilayers and micelles than S-type CTXs (*4*) and will redistribute themselves between the penetrating and peripheral binding states under certain experimental conditions (*5*). Several P-type CTXs have been demonstrated to be hemolytic (*4*) and also to induce reversible formation of an extra outwardly rectifying conductance in bullfrog atrial myocytes (*6*). Comparison of the three-dimensional (3D) structures determined in a hydrophobic environment for two P-type CTXs, i.e., CTII from *Naja oxiana* and CTX A5 from *Naja atra*, has suggested that the membrane binding regions of P-type CTXs involve the hydrophobic residues located near the tips of all three loops (*7*, *8*). In earlier studies, fluorescence and NMR spectroscopy have been extensively used to investigate other P-type CTXs such as CTX A3 from *N. atra* and Tγ from *Naja nigricollis*, and the results suggest the involvement of similar regions for membrane lipid binding (*5*, *9*). When the fact that the available 3D structures of CTXs are all β-sheets with four disulfide bonds is considered, it is not clear how the amphiphilic polypeptides such as P-type CTXs can adopt different conformations suitable for both aqueous and hydrophobic environments. It was also unclear how such structures are modulated to achieve the reversible redistribution between the peripheral and penetrating membrane binding modes required for their general cytotoxic effect.

Recent X-ray diffraction and NMR studies of P-type CTXs in which the three loops were exposed to a hydrophobic environment, either by the hydrophobic contact between the hydrophobic amino acid residues under crystal packing conditions or by binding to perdeuterated dodecylphosphocholine (DPC) micelles in aqueous solution, indicate the presence of one or two bound waters near the tip of loop II (*7*, *8*, *10*). One water molecule is structurally conserved and forms hydrogen bonds to the NH proton of Met26 for CTII and Leu27 for CTX A5. The bound water plays a delicate structural role in the formation of the membrane binding motif by forcing the tip of loop II to form an ω shape resulting in the bridging of the other two hydrophobic domains at loops I and III (*8*). In fact, the NMR chemical shifts of the amide proton of Met26 undergo the most significant downfield shift upon the binding of CTII and Tγ to DPC micelles. This observation is consistent with the formation of a stronger hydrogen bond between the amide proton of Met26 and the bound water within a hydrophobic micellar environment as compared to within an aqueous

† This work was supported by a grant from the National Science Council, Taiwan (NSC 89-2113-M-007-048 and NSC 89-2311-B-007-045), and an NSC-NRC Joint Research Project grant (N-001).

* To whom correspondence should be addressed: Department of Life Sciences, National Tsing Hua University, Hsinchu 30043, Taiwan. Telephone: +886 3 5742752. Fax: +886 3 5715934. E-mail: wgwu@life.nthu.edu.tw.

‡ National Tsing Hua University.

§ National Research Council.

[1] Abbreviations: CTX, cardiotoxin; DPC, dodecylphosphochline; 3QF, triple-quantum filtered; FID, free induction decay; NMR, nuclear magnetic resonance; NOE, nuclear Overhauser effect; ROE, rotating frame Overhauser effect; NOESY, nuclear Overhauser effect spectroscopy; ROESY, rotating frame Overhauser effect spectroscopy; TOCSY, total correlation spectroscopy; DQF-COSY, double-quantum filtered correlated spectroscopy; rmsd, root-mean-square deviation.

10.1021/bi010848f CCC: $20.00
Published on Web 10/06/2001

solution (*7*, *9*). This is of prime concern since it had been previously proposed that a membrane protein may redistribute itself between penetrating and peripheral binding states, if the activity of the bound water buried in the interior turns of globular proteins can be regulated (*11*). Therefore, it is important to characterize both the structure and dynamics of the P-type CTXs, especially at the water binding loop region, to gain a better understanding of the relationship between their structure and function. So far, there is no report on the residence time of the bound water and the backbone dynamics of the P-type CTX.

In the work presented here, multinuclear NMR studies were performed on the major CTX from *N. atra*, i.e., P-type CTX A3, at pH 6.0 in phosphate buffer. Two-dimensional ^{1}H NOESY and ROESY NMR analyses allowed not only the determination of its 3D structure but also the identification of the exact location of the bound water (*12*, *13*). To characterize the motional properties of the bound water, the motional properties of the peptide backbone were also investigated using a model-free analysis of the ^{13}C NMR spin−lattice relaxation time, T_1, and ^{13}C{^{1}H} nuclear Overhauser effect (NOE) obtained at natural abundance (*14*, *15*). The order parameter, S^2, of the polypeptide backbone and overall correlation time, τ_R, of the relatively flat CTX A3 are presented. Recent advances in the relaxation-dispersion measurements (*16*, *17*) and triple-quantum filtered (3QF) NMR of $H_2{}^{17}O$ (*18*−*24*) in the presence of biological macromolecules allowed the determination of the residence time and the total number of bound water molecules. In the study presented here, 3QF ^{17}O NMR was used in conjunction with ^{13}C NMR relaxation data to establish further the existence of a bound water molecule. The results indicate that a single water molecule is hydrogen bonded to the NH of Met26 in the aqueous state with a lifetime that is longer than the isotropic tumbling time (3.8−4.5 ns) of the CTX A3 molecule. Interestingly, unlike previously identified long-lived (longer than a nanosecond) bound water molecules, which are usually found in the internal cavity of proteins such as the four buried bound waters in BPTI (*18*, *25*, *26*), the one identified in the P-type CTXs is not buried and can form hydrogen bonds with other surface water molecules. The significance of this observation is discussed within the context of the mechanism of regulating the membrane binding mode of amphiphilic polypeptides by water molecules.

EXPERIMENTAL PROCEDURES

Sample Preparation. CTX A3 from *N. atra* and Tγ from *N. nigricollis* (Sigma Chemical Co., St. Louis, MO) were purified by SP-Sephadex C-25 ion exchange column chromatography followed by HPLC on a reverse-phase C-18 (10 mm) column as described previously (*3*). The purity of both toxins was checked by SDS−polyacrylamide gel electrophoresis, and it was found to be higher than 99%. The pH of the sample was controlled at 6.0 ± 0.1 with 10 mM phosphate buffer. Toxin concentrations of 5, 5, and 28 mM were used for ^{1}H, ^{13}C, and ^{17}O NMR experiments, respectively. There was no indication of protein aggregation or degradation as judged by the ^{1}H NMR spectral quality during the experiments (up to 50 °C for 1 week) and sample storage time (several months at 4 °C). The pH of the sample containing 100% D_2O was corrected according to the isotope effect of pD = pH* + 0.4.

NMR Spectroscopy. All ^{1}H NMR experiments were carried out on a Bruker DRX600 spectrometer equipped with a 5 mm triple-resonance probe. Two-dimensional ^{1}H spectra of COSY, DQF-COSY, TOCSY (70 and 90 ms mixing times), NOESY (50, 75, and 150 ms mixing times), and ROESY (75 and 150 ms mixing times) were obtained at 27 °C as described previously (*27*−*29*). Water suppression was achieved by either a pulsed field gradient with the 3-9-19 WATERGATE sequence or presaturation. For detection of bound water, NOESY and ROESY spectra, with the same mixing time of 75 ms, were acquired at various temperatures (5, 27, and 45 °C), as described previously (*12*, *13*). Chemical shifts were referenced to tetramethylsilane (TMS). All spectra were typically acquired with 2048 complex data points in the t_2 dimension and 512 points in the t_1 dimension.

The T_1 and ^{13}C{^{1}H} NOE were measured in duplicate and at two magnetic fields (9.4 and 14 T) as described by Kay and co-workers (*14*, *15*) using Varian INOVA 400 and 600 spectrometers. Typically, T_1 measurements consisted of five or six recovery times with each spectrum having 256 transients of 1024 data points in the t_2 dimension and 32 t_1 increments with a recycle delay of 1.1 s. Processing was done with extrapolation in the t_1 dimension by linear prediction to 128 complex points followed by zero-filling to 2048 points and apodization with a Gaussian function in both dimensions prior to Fourier transformation. The ^{13}C T_1 values were obtained by exponential fits of the integrated $^{13}C_\alpha$ cross-peaks using standard Varian software.

3QF transverse ^{17}O relaxation measurements were performed at 22 °C on a 20% w/v (28 mM) solution of CTX A3 in D_2O (20 at. % ^{17}O). Measurements were performed at 81.35 MHz (14 T) on a Varian INOVA 600 spectrometer with a Bruker 5 mm broadband probe using the pulse sequence and phase cycling described by Chung and Wimperis (*23*): $90^o_\phi - t_1/2 - 180^o_\phi - t_1/2 - 70.5^o_{\phi+90} - t_m - 90^o_0$ − Acq. with t_m set to 10 μs and a phase cycling of 96 steps. The first 90° pulse generates observable first-rank single-quantum coherence that relaxes partly into third- and fifth-rank single-quantum coherence during the time t_1. The 180° pulse removes chemical shift and offset effects during t_1. The 70.5° pulse converts the third-rank single-quantum coherence into triple-quantum coherence, which is only allowed to evolve for a short time (t_m) before conversion back to third-rank single-quantum coherence for detection. During the acquisition time, the third-rank single-quantum coherence evolves into an observable signal as a result of quadrupolar relaxation. The phase cycle of the pulses and the receiver ensure that only the three-quantum signal is detected. Data were acquired with a spectral width of 50 kHz, 1024 complex points, a repetition time of 85 ms, and 19 200 transients. No apodizaton of the FID was used prior to a 2048-point Fourier transformation. The evolution time of t_1 ranged from 32 μs to 2 ms.

Spatial Structure Determination. Three-dimensional conformers were calculated using NMR constraints in the simulated annealing protocol of the program X-PLOR (version 3.01) (*30*) on a Silicon Graphics O2 workstation. Twenty low-energy conformers were selected from 50 calculated structures for the final structural analysis. The

values of NOE energy and Cdih energy were calculated with force constants of 50 kcal mol^{-1} Å^{-2} and 50 kcal mol^{-1} rad^{-2}, respectively. The Insight II software was used to display and analyze the structural results.

The ^{1}H NOE constraints were estimated from a 50 ms NOESY spectrum and classified into three groups: weak (3.4 ± 1.6 Å), medium (2.7 ± 0.9 Å), and strong (2.3 ± 0.5 Å). Weak NOE peaks that can only be detected by NOESY with a 150 ms mixing time provided the upper bound constraints are up to 6 Å. Calibration of the NOE distance constraint was carried out by using the known atomic distances of 2.5 Å between the [2,6] and [3,5] proton pairs of the tyrosine aromatic ring. The hydrogen bonds forming antiparallel β-sheet were identified as the slowly exchanging backbone amide protons. The hydrogen bond constraints between the amide proton and oxygen were defined as 2.0 ± 0.3 Å. Constraints of 2.01−2.03 Å for the distances between two sulfur atoms of the four disulfide linkages were applied. Forty dihedral angle restraints were derived from $^3J_{NH-\alpha H}$ coupling constants measured by DQF-COSY. $^3J_{NH-\alpha H}$ coupling constants of <6 Hz were defined in the interval of −60 ± 20°. $^3J_{NH-\alpha H}$ coupling constants of >8 Hz were constrained in the interval of −120 ± 70°, and those greater than 10 Hz were constrained in the interval of −120 ± 20°.

The 20 low-energy structures and NMR constraints have been deposited in the RCSB Protein Data Bank (entry 1I02), and the chemical shifts have been deposited in the BioMagnetic Resonance Bank (entry 4966).

Proton Chemical Shift Analysis. The theoretical proton chemical shifts of the $C_\alpha H$ of CTX A3 were obtained according to the method published by Williamson and Asakura (*31*) and Asakura et al. (*32*) as described in our previous study of the pH-dependent conformational change of P-type CTX A5 (*8*). Briefly, three shielding effects, the ring current effect, the electric field effect, and the magnetic anisotropy effect, were estimated and calculated using the coordinates of the CTX A3 structure.

^{13}C Relaxation Analysis. The ^{13}C relaxation data as measured by double-INEPT type inverse-detected experiments with suppression of cross-correlation and cross-relaxation (*14*, *33*) were analyzed using a model-free approach (*34*). It was assumed that relaxation was purely through the ^{1}H−^{13}C mechanism so that the spin−lattice relaxation rate and NOE for a protonated carbon are given by

$$\frac{1}{T_1} = \frac{\hbar^2 \gamma_H^2 \gamma_C^2}{4 r_{CH}^6}[J(\omega_H - \omega_C) + 3J(\omega_C) + 6J(\omega_H + \omega_C)] \quad (1)$$

$$\mathrm{NOE} = 1 + \frac{\gamma_H[6J(\omega_H + \omega_C) - J(\omega_H + \omega_C)]}{\gamma_C[J(\omega_H - \omega_C) + 3J(\omega_C) + 6J(\omega_H + \omega_C)]} \quad (2)$$

where r_{CH} is taken to be 1.09 Å, $\hbar$ is Planck's constant, ω_H and ω_C are the Larmor frequencies in radians per second, and γ_H and γ_C are the magnetogyric ratio for a proton and carbon, respectively. Within the framework of the model-free analysis, the spectral density function describing both internal and global motions is given for potentially anisotropic overall rotational diffusion motion by

$$J(\omega) = \frac{2}{5}\left\{2S^2\left[\frac{A\tau_1}{1+\omega^2\tau_1^2} + \frac{(1-A)\tau_2}{1+n\omega^2\tau_2^2}\right] + 2(1-S^2)\left[\frac{\tau_{1e}}{1+\omega^2\tau_{1e}^2} + \frac{\tau_{2e}}{1+\omega^2\tau_{2e}^2}\right]\right\} \quad (3)$$

where $1/\tau_{1e} = 1/\tau_1 + 1/\tau_i$ and $1/\tau_{2e} = 1/\tau_2 + 1/\tau_i$, where τ_1 and τ_2 represent the two correlation times describing the overall reorientation of the molecule and A is a mixing coefficient which ranges from 0 to 1. The generalized order parameter S describes the spatial restriction of the internal motions of $C_{\alpha i}$, which have an effective correlation time τ_i. In the case of isotropic overall reorientation, $\tau_1 = \tau_2$ and eq 3 simplifies to that given by Lipari and Szabo (*34*) for isotropic overall motion. In the study presented here, no assumption was made as to the nature of the overall reorientation (i.e., isotropic was not assumed) or to the rate of motion. Thus, the anisotropic form of the spectral density function depends on three global parameters [A ($0 < A < 1$), τ_1, and τ_2] and two local parameters [S ($0 \le S \le 1$) and τ_i] for each position. The data were fitted by a least-squares method as described previously (*35*, *36*).

^{17}O Relaxation Analysis. To probe the existence of bound water, ^{17}O relaxation experiments could be used to detect the property of the bound water in the presence of an ~5000-fold excess of bulk water. Several recent studies have been published in which bound water has been detected by ^{17}O relaxation experiments (*18*−*22*). We therefore explored these ^{17}O relaxation experiments as a way of providing additional evidence of a CTX A3-bound water molecule. The general theoretical framework for multiquantum filtered quadrupolar relaxation for spin = $^5/_2$ nuclei has been described in detail by Chung and Wimperis (*23*). For completeness, we summarize below several key points in the paper by Chung and Wimperis to provide background information for the relaxation analysis related to this work.

Wimperis and co-workers have shown that for pure quadrupolar relaxation spin = $^3/_2$ and $^5/_2$ nuclei undergoing isotropic motion outside the motional narrowing regime ($\omega_o\tau_c > 1$) the degenerate single-quantum coherences relax at different rates (*23*, *24*). In the case of ^{17}O (spin = $^5/_2$), relaxation becomes triexponential. As a result, after an initial $\pi/2$ pulse, transverse relaxation causes the initial in-phase single-quantum coherence described by the first-rank tensor operators ($T_{1,+1}$ and $T_{1,-1}$) to relax partly into antiphase third-rank (given by tensor operators $T_{3,+1}$ and $T_{3,-1}$) and fifth-rank (given by tensor operators $T_{5,+1}$ and $T_{5,-1}$) single-quantum coherences. The third- and fifth-rank single-quantum coherences do not contribute to the ^{17}O line shape in a conventional pulse-acquire experiment but may be measured using multiple-quantum filtration techniques. Thus, for motionally hindered water molecules, triexponential ^{17}O relaxation allows the detection of water bound to macromolecules in the presence of bulk water which exhibits rapid motion and monoexponential ^{17}O relaxation. Using the pulse sequence of Chung and Wimperis (*23*) described above and the phase cycle, ϕ, chosen to select for triple-quantum coherence, the third-rank single-quantum coherence arising from transverse relaxation during t_1 is transformed into triple-quantum coherence. During acquisition, the third-rank single-

quantum coherence generated by the last pulse partially relaxes into in-phase detectable first-rank single-quantum coherence ($T_{1,+1}$ and $T_{1,-1}$). The measured signal intensity from the 3QF transverse measurement is given by

$$I(t_1) = {}^5/_6 I_o\, f_{31}(t_1)\, f_{13}(t_2) \quad (4)$$

where I_o is the total equilibrium signal intensity as measured by a single $\pi/2$ pulse under identical experimental conditions. The functions $f_{31}(t_1)$ and $f_{13}(t_2)$ are triexponential functions that give the amplitude of the transfer between third- and first-rank single-quantum coherence resulting from quadrupolar relaxation during the evolution and detection periods, respectively. Since only motionally hindered water can give rise to the triple-quantum coherence, information about water bound to macromolecules can be obtained by evaluating $f_{31}(t_1)$ and $f_{13}(t_2)$.

If it is assumed that bound water exhibiting triexponential ^{17}O relaxation is in fast exchange with bulk water exhibiting monoexponential relaxation, transverse relaxation of the bulk water is given by the relaxation matrix

$$\mathbf{R}_{bulk} = p_f \mathbf{R}_{free} + p_b \mathbf{R}_{bound} \quad (5)$$

where p_f and p_b are the fractions of free water and bound water, respectively. $\mathbf{R}_{free}$ is the 3×3 relaxation matrix for free water, which is assumed to be undergoing fast motion ($\omega_o\tau_c \ll 1$) and is thus diagonal. $\mathbf{R}_{bound}$ is the 3×3 relaxation matrix describing quadrupolar relaxation for single-quantum coherences with odd rank. The elements of the relaxation matrix depend on the spectral densities J_0, J_1, and J_2 and the quadrupolar coupling constant $(e^2qQ/h)(1 + \eta^2/3)^{1/2}$. In the study presented here, the quadrupolar coupling constant that was used equaled 7.6 MHz. A previous study has indicated that the ^{17}O quadrupolar coupling constants for free and protein-bound water are nearly equal and have values of 7.6 MHz as has been used previously (*21*). However, more recently, a value of 6.5 MHz has been used (*22*) for the quadrupolar coupling constant of free water and that bound to protein. The time course as described by the function $f_{13}(t)$ in eq 4 can be evaluated as described previously (*21*, *23*) by diagonalizing $\mathbf{R}_{bulk}$ to obtain the diagonal eigenvalue rate matrix and the associated eigenvector matrix, **V**. The amplitudes of the exponential decays relating to the transfer between the single-quantum coherence l and l' (l and l' have values of 1, 3, or 5) are derived from **V** according to $a_{l'l,q} = V_{ql'}V_{ql}$ (where q has values of 1−3) (*21*, *23*). The amplitude factors $a_{l'l,q}$ are functions of $\omega_o\tau_c$. In this study, the temporal dependence of the third-rank single-quantum coherence is of interest and is given by

$$f_{31}(t) = f_{13}(t) = V_{13}V_{11}\exp(-R_1t) + V_{23}V_{21}\exp(-R_2t) + V_{33}V_{31}\exp(-R_3t) = a_{31,1}\exp(-R_1t) + a_{31,2}\exp(-R_2t) + a_{31,3}\exp(-R_3t) \quad (6)$$

$\mathbf{R}_{free}$ can be constructed from the T_1 of free water (*23*). Thus, by varying τ_c and p_b, we can calculate the transfer function $f_{31}(t)$ according to eq 6 that gives the best fit to the experimental results.

In the case presented here, ^{13}C NMR relaxation studies indicate that there is fast internal motion in the region where the water molecule is thought to bind. Such internal fast motion would influence the relaxation rates for bound water. We have adapted the spectral densities to include the possibility of such internal motion by using the modified formalism

$$J_n = \frac{2\tau_c S^2}{1 + n\omega_o{\tau_c}^2} + \frac{2\tau_e(1 - S^2)}{1 + n\omega_o{\tau_e}^2} \quad (7)$$

where τ_c is the correlation time of the bound water molecule, ω_o is the Larmor frequency of ^{17}O, S is the generalized order parameter averaged by fast internal motion, and τ_e is the effective correlation time for internal motion. ^{13}C relaxation results (see the Results) indicate that τ_e is expected to have a value of 20 ps and an S^2 of 0.7.

The data in Figures 8 and 9 were iteratively fit by constructing trial relaxation matrixes, $\mathbf{R}_{bulk}$, by varying the fraction of water bound (p_b) to CTX A3 and the correlation time (τ_c) of the complex. The rate matrix, $\mathbf{R}_{free}$, for free water was constructed from the ^{17}O T_1 of the bulk water as described elsewhere (*23*). The ^{17}O relaxation rate of water was measured by a standard inversion recovery experiment and found to be 330 s^{-1}. The resulting trial rate matrix was diagonalized using standard methods (*37*). Trial matrixes were constructed from spectral densities calculated using eq 7 with S^2 having values of 1.0 and 0.7 and an internal correlation time of 20 ps. The dependence of the 3QF signal amplitude on the evolution time was fit by a least-squares simplex minimization of the difference between the calculated and experimental amplitudes according to

$$\text{error} = \sum \frac{[I(t_1)_{exp} - {}^5/_6 I_o f_{31}(t_1)_{cal}]^2 I(t_1)_{exp}}{I_{max}} \quad (8)$$

where I_{max} is the maximum signal amplitude in the series of spectra. The FID in Figure 9 was fit according to

$$\text{error} = \sum \frac{[I(t_2)_{exp} - {}^5/_6 I_o f_{31}(t)_{cal} f_{13}(t_2)_{cal}]^2 I(t_2)_{exp}}{I_{max}} \quad (9)$$

where t had a value of 1.4 ms. Such fitting of 3QF relaxation data assumes that all of the signal intensity arises only from the selection of triple-quantum coherence. Thus, for sufficiently small values of t_1 and t_2, the signal amplitude is expected to be nearly zero. Inspection of Figures 8 and 9 indicates that even at short times (<100 μs) the signal intensity is significant. Although care was taken to carefully adjust pulse lengths and receiver gain to minimize signals that do not arise from the 3QF signal, it proved to be impossible to reduce the residual non-3QF water signal.

Molecular Dynamics Simulation. Molecular modeling was conducted using the Discovery 3.0 module of Insight II 95.0 on a SGI O2 workstation. The coordinate of the CTX A3 structure with one bound water molecule was directly soaked with a 5 Å water layer (603 water molecules). The AMBER force field was chosen to define the charge distribution and interaction energies. The nonbonded cutoff value was set at 15 Å. Three hundred steps of energy minimization were performed initially to remove improper atom contacts and forces. A total 500 ps molecular dynamics simulation was

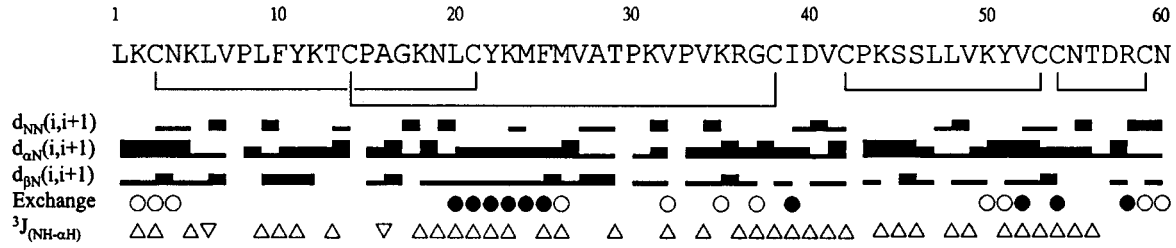

FIGURE 1: Summary of the ^{1}H NMR data of CTX A3. The sequence of CTX A3 is shown at the top. Connecting lines below the sequence represent disulfide bridges. The relative intensities of sequential NOEs, classified as weak, medium, and strong, are represented by the thickness of filled bars. Amide protons that still can be observed after 12 h in a D_2O solution at pH 6.0 are marked with black circles, and those that can be observed from the beginning to several hours are marked with white circles. $^3J_{NH-\alpha H}$ coupling constants of >8 (△) and <6 Hz (▽) are labeled.

conducted using a 1 fs time step with the coordinates of CTX A3 and water molecules saved at intervals of 5 ps.

RESULTS AND DISCUSSION

^{1}H NMR and CTX A3 Solution Structure. Although the solution structure of CTX A3 at pH 3.0 has been determined previously by ^{1}H NMR (*38*), it was later demonstrated that the structure was based on at least nine wrongly assigned NH signals out of the 60 amino acid residues (*39*). As a result, the existing CTX A3 structure could not be used for the study of the structures and dynamics of the water binding loop in the P-type CTX A3. In the study presented here, the correct assignments of all proton resonances (except the NH proton of Leu1) of CTX A3 were achieved using the well-established sequential assignment method based on the information obtained from the DQF-COSY, TOCSY, and NOESY spectra of the toxin at pH 6.0 and 27 °C. The structure of CTX A3 was determined on the basis of a total of 680 NOE and 40 dihedral constraints (see Figure 1 for a summary of the ^{1}H NMR data). Twenty lower-energy structures were obtained from 50 starting structures with no violation of NOE constraints larger than 0.2 Å and a backbone rmsd of <0.7 Å (Table 1), indicating that the CTX A3 structure is defined well by the NMR data.

CTX A3 is a typical three-fingered snake toxin formed entirely by five antiparallel β-sheets (double-stranded β-sheet for amino acid residues 2−4 and 11−13 and triple-stranded β-sheet for residues 20−26, 35−39, and 49−54). It consists of three-finger tips with loops termed loops I (residues 5−10), II (residues 26−34), and III (residues 46−49) that protrude from a central core, tightened by four disulfide bonds (Figure 2A). Both the tips of loop I and loop II bend toward the same side of the C-terminal loop and form a concave surface giving a flat shape to the CTX A3 molecule. In this aspect, the structure of CTX A3 is essentially the same as the structure of the major form of CTII from *N. oxiana* with the trans conformation of the Val7−Pro8 bond (*40*). The structure of the minor form of CTII having a cis conformation of the Val7−Pro8 bond forces the tip of loop I to protrude toward the opposite direction on the convex side.

It is interesting to point out that, like CTII, a minor form of CTX A3 can also be detected at <10 °C (data not shown). However, as judged by the chemical shift difference of the two forms, the structural differences between the major and minor forms of CTX A3 are located mainly in the core and in the triple-stranded β-sheet, instead of the loop I region. CTX A3 and CTII differ by only two amino acid residues near loop I, i.e., Asn4 versus Lys4 and Tyr11 versus Ser11. The latter indicates that the structure and dynamics of the functionally important thumb−finger region are highly sensitive to its exact amino acid sequence.

Table 1: Input Data and Structural Statistics[a] for the Solution Structure of CTX A3

input data for X-PLOR	
no. of dihedral constraints	40
no. of NOE constraints	680
no. of long-range constraints (range, ≥5)	189
no. of medium-range constraints (range, <5)	49
no. of sequential constraints (range, 1)	179
no. of intraresidual constraints (range, 0)	263
no. of hydrogen bonds	19
no. of disulfide bonds	4
rmsds (Å)	
backbone	0.64 ± 0.11
heavy atoms	1.02 ± 0.11
side chains	1.31 ± 0.14
energy term (kcal/mol)	
overall energy	176.7 ± 4.5
bond energy	6.4 ± 0.2
angle energy	132.9 ± 1.8
improper energy	13.9 ± 0.8
Vdw energy	12.4 ± 2.6
NOE energy	11.1 ± 1.8
rmsd from idealized geometry	
bonds (Å)	0.003 ± 0.000
angles (deg)	0.699 ± 0.005
improper angles (deg)	0.435 ± 0.014
Ramachandran plot	
most favorable regions (%)	73.1 ± 5.4
additionally allowed regions (%)	25.8 ± 5.4
generously allowed regions (%)	0.8 ± 0.9
disallowed regions (%)	0.3 ± 0.7
average *G*-factors derived from PROCHECK-NMR	
$\phi-\psi$	−0.94 ± 0.14
$\chi_1-\chi_2$	−1.69 ± 0.15

[a] Structural statistics, including rmsd, energy terms, and *G*-factors, were derived from 20 lower-energy conformers from 50 simulated annealing structures.

As for most published CTX structures [except CTX A2 from *N. atra* (*41*)], the ϕ and ψ dihedral angles of the polypeptide backbone of CTX A3 fall within a reasonable region of a Ramachandran plot (Figure 3A). In addition, chemical shift analysis of the C_α protons resonances based upon the NMR structures (Figure 2A) and using theoretical considerations involving the electrostatic and ring current shift effects indicated that the orientation of aromatic side chains and the overall 3D structure of the molecule are generally correct (Figure 3B). With the exception of Thr13, Tyr22, and Arg58, excellent correlations are observed between experimental and theoretical results.

The inconsistency between the theoretical and experimental data of the C_αH of Thr13 and Tyr22 most likely reflects

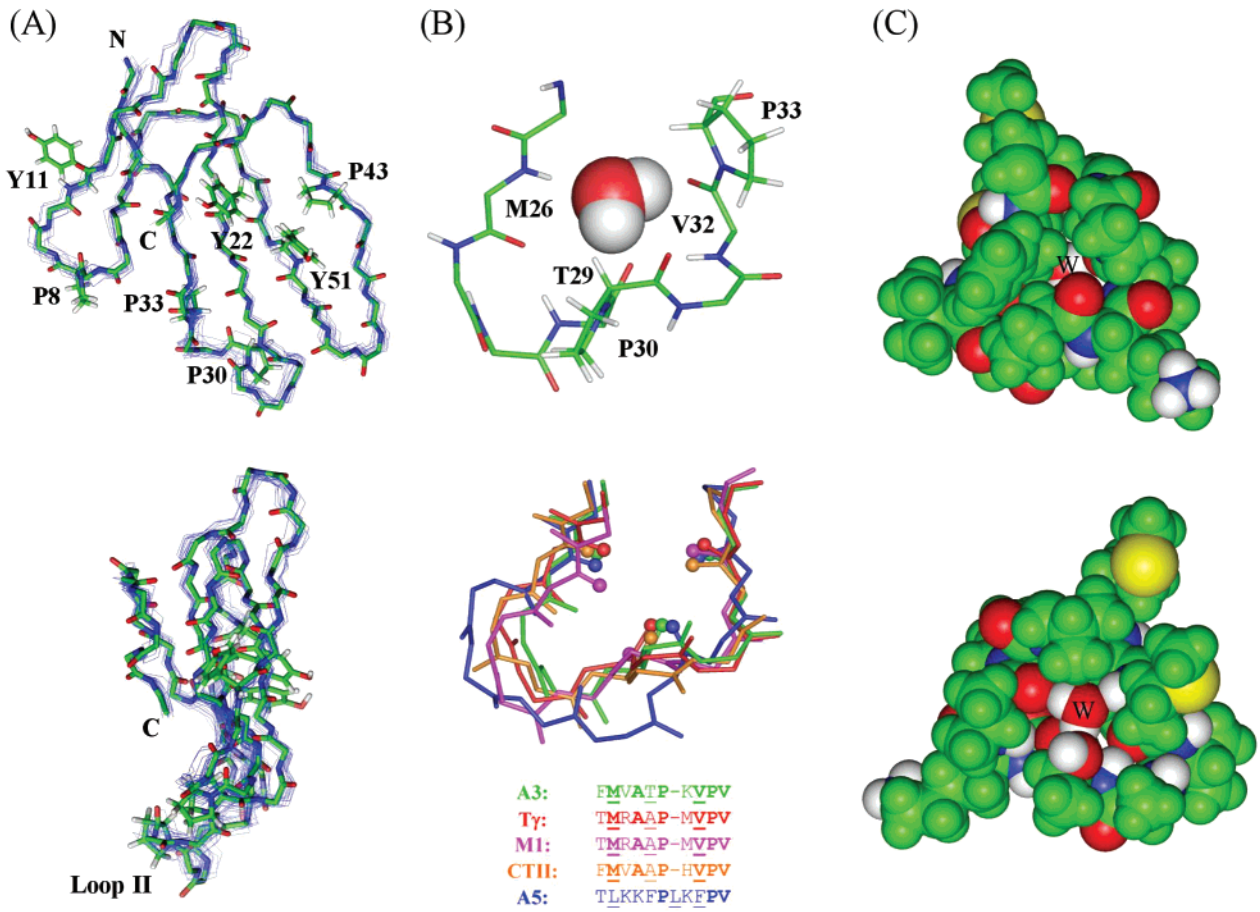

FIGURE 2: (A) Illustration of the overall structure of CTX A3. The thin lines demonstrate the superposition of the backbone traces from 20 selected low-energy solution structures of CTX A3. The final averaged structure is drawn in stick mode and stacked together. (B) Interaction of bound water with amino acid residues located near the tip of loop II of CTX A3 (top). Comparison of the loop II structures and sequences of five selected P-type CTXs, including A3, Tγ, M1, CTII, and A5 (bottom). (C) CPK model of the loop II structure as viewed from the concave and the convex side to emphasize the accessibility of water to the region. The hydrophobic region is colored green, and other atoms are colored according to atom type (blue, nitrogen; yellow, sulfur; red, oxygen; and write, hydrogen).

the insufficient consideration of the electrostatic and ring current shift effects for the two nearby Tyr side chains under an extremely different environment. The Tyr22 aromatic ring sits right in the center of the core and lies on top of the triple-stranded β-sheet to form an angle of $\sim$100° with the β-sheet (see Figure 2A). Examination of the eight X-ray and NMR structures, including M1, M3, Tγ, A1, A2, A5, CTII, and A3 (this study), indicated that such an orientation is well-conserved with a $\alpha H-C_\alpha-C_\beta-C_\gamma$ dihedral angle of $-159 \pm 2°$ (except for a value of approximately $-120°$ found for that of CTX A2 from *N. atra*). This observation indicated that Tyr22 is located in a conserved region of the toxins and exhibits a conserved local structure in CTX structures. In contrast, Tyr11 is highly disordered and appears to be exposed to the aqueous environment. This observation explains why the experimental chemical shifts of Thr13 and Tyr22 deviate the most from calculated chemical shifts as seen from the linear correlation curve (inset of Figure 3B). The case for Arg58 can also be understood since it is the only residue with ϕ and ψ angles falling in the left-hand helix region.

^{13}C NMR and Backbone Dynamics for CTX A3. Once the ^{1}H resonances were correctly assigned, the ^{13}C chemical shifts were determined from an HSQC experiment (*42*). As shown in Figure 4, all C_α resonances could be assigned except for those of Lys12 and Leu20, since their $C_\alpha H$ resonances had the same chemical shift as the water signal. However, due to the overlap of resonances, only 47 of 60 C_α resonances could be used reliably for the analysis of the relaxation data.

CTX A3 was found to tumble isotropically when using the model-free formalism in which the possibility of global anisotropic motion was allowed. The T_1 and NOE data measured in duplicate at 9.4 (400 MHz) and 14 T (600 MHz) were thus analyzed. Two correlation times and a weighting factor, *A*, which expresses the relative contribution of these correlation times (eq 3) were determined. Note that an *A* value of 1.0 is indicative of isotropic motion. The data obtained at 9.4 T gave an overall correlation time, τ_R, of 3.8 ns and a global anisotropic factor, *A*, of 0.98. A slightly higher τ_R value of 4.5 ns, with essentially the same *A* value of 0.98, was calculated for the data obtained at 14 T. The exact reason for the small discrepancy of the correlation times estimated between the two NMR fields is not known at this time. However, in virtually all of the fits, the two correlation times that define potential anisotropic motion differed by less than 10%, indicative of isotropic tumbling. Thus, interpretation of NOE data assuming an isotropic motional model of a flat CTX molecule is justified for further studies.

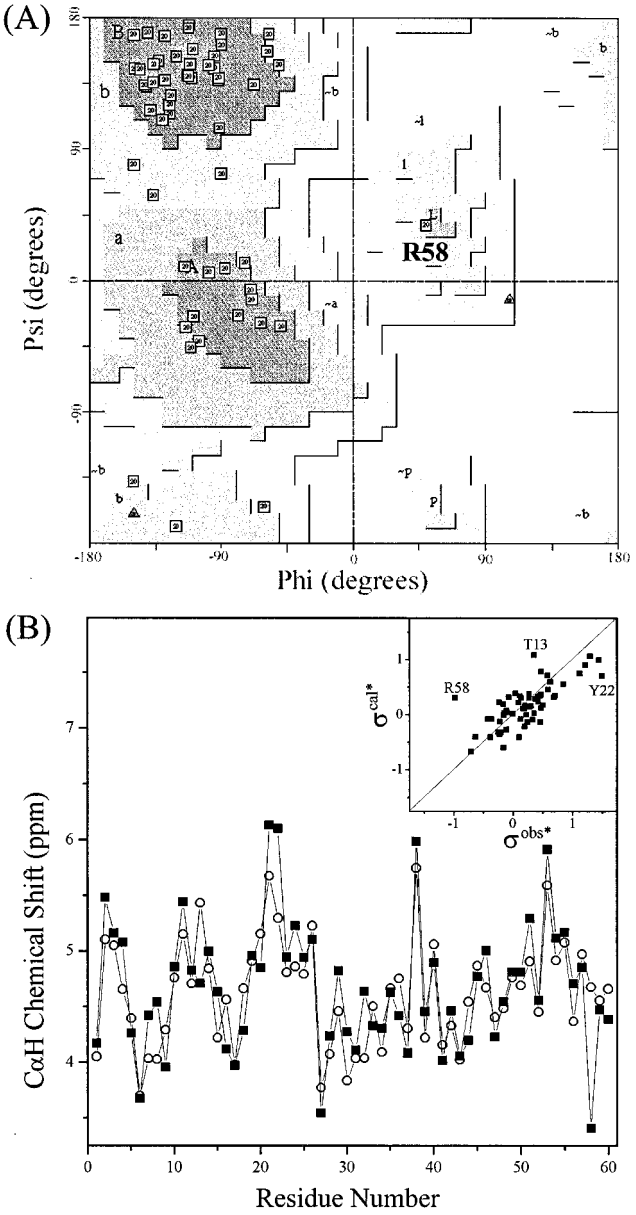

FIGURE 3: (A) Ramachandan plot of the CTX A3 structure (PROCHECK-NMR, version 3.4.3). Glycines are labeled with triangles and all other residues with squares. The residue (Arg58) is the only residue located in the left-handed α-helix region and labeled specifically. (B) Plot of the sequence dependence of the calculated (○) and experimental (■) chemical shifts of the $C_\alpha H$ proton. The inset expresses the close relationship between the experimental σ^{obs*} ($\sigma^{obs*} = \sigma^{obs} - \sigma^{random\ coil}$) and theoretical σ^{cal*} ($\sigma^{cal*} = \sigma^{cal} - \sigma^{random\ coil}$). Positive and negative values represent the downfield and upfield chemical shifts, respectively. The three amino acid residues (Thr13, Tyr22, and Arg58) depicted in the inset are those that deviate the most between the experimental and theoretical values.

The correlation time estimated by the NMR method is known to be higher than that estimated by other methods presumably due to the high protein concentration used in the NMR study. Previously, a correlation time of ~3.3 ns for 2 μM CTX M1 or Tγ was obtained by measuring fluorescence natural decay lifetimes (*43*). In contrast, a τ_R value of 5.5 ns was obtained from 25 mM BPTI, a 58-amino acid protein with a molecular weight similar to that of CTX, at pD 4.5 by ^{13}C relaxation (*44*). Therefore, the overall tumbling motion of the CTX A3 molecule can be safely concluded to be essentially isotropic with a correlation time of ~3.8−4.5 ns as estimated by ^{13}C NMR relaxation.

The polypeptide backbone dynamics of CTX A3 could be observed from a comparison of the NOE constraints, rmsd values, and S^2 values (Figure 5). In general, C_α positions exhibiting high S^2 values (>0.9) and clustered within domains of the peptide sequence may be taken to reflect rigid regions of structure. Five of the C_α positions in the polypeptide backbone have S^2 values of >0.9 as indicated by the asterisks shown in Figure 5C. Except for Val27, the other four residues (Tyr22, Cys38, Cys53, and Arg58) correspond well to the local minimum of the root-mean-square deviation (rmsd) of the 20 calculated 3D structures (Figure 5B). Val27 is located within a dynamic region corresponding to lower S^2 values centered at loop II (residues 26−34). It is also noteworthy that more long-range NOEs were also observed around those regions exhibiting the high S^2 values. In addition, some of the S^2 values for certain residues corresponded nicely to their respective packing environment. For instance, as shown in Figure 2A, Tyr22, which is located right at the center of the hydrophobic core, has an S^2 value of ~0.98, while Tyr11, which is protruding into the aqueous environment, has an S^2 value of ~0.7. Tyr51, with its aromatic ring facing Pro43 as evidenced by the unusual chemical shifts of 0.37 and 0.56 ppm for one H_β and one H_γ proton of Pro43, respectively, appears to have an S^2 value (~0.85) falling between those of the other two Tyr residues.

Emphasis has been placed on that fact that there is no strict correlation between the backbone dynamics as reflected by S^2 values and the backbone structural resolution as determined by the rmsd calculated from the ensemble of acceptable NMR solution structures. The structural resolution (as defined by the rmsd) is sensitive to both fast and slow motion, where the values of S^2 are a function of rapid motions only. In fact, it has been known for some time that the values of T_1 and S^2 obtained from either ^{15}N or ^{13}C NMR relaxation measurement do not show any correlation with X-ray crystallographic *B* factors (*45*, *46*). This is particularly evident with the first 13 amino acid residues near the N-terminus. The S^2 values of Cys3, Asn4, and Tyr11 can be considered to be abnormally low since their corresponding rmsd indicated that they are located in a structurally restricted region. The lack of good correlation between the NMR relaxation data and the structural resolution in the first loop of the other three-finger toxins, i.e., toxin α from *N. nigricollis* and S-type CTX II from *N. atra*, has also been reported (*47*, *48*). In the following, we focus on the structures and dynamics of the water binding loop located near the tip of loop II.

Water Binding Loop and Molecular Dynamics Simulation. The X-ray structures revealed the presence of one and two bound water molecules in Tγ from *N. nigricollis* (*10*) and CTX A5 from *N. atra* (*8*), respectively, located near the tip of loop II. In the previous NMR structural report of CTX M1 (CTX IIb), the NH of Met26 was reported to have a slow exchange rate (10^{-3}−10^{-5} min^{-1}) and to lack suitable hydrogen bond acceptors in loop II (*49*). Recent ^1H NMR studies on CTII from *N. oxiana* in both aqueous and micellar environment have further shown that the existence of the bound water in the more flexible region of the loop is not an artifact due to the crystal packing, since it can also be

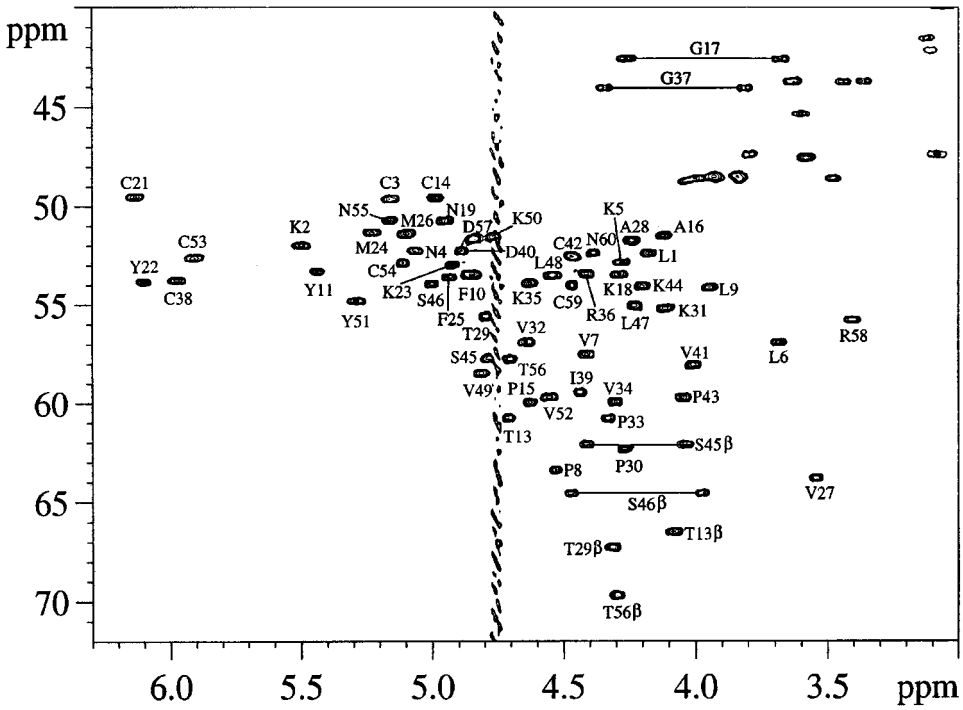

FIGURE 4: $^{1}H-^{13}C$ HSQC spectrum of the naturally abundant $C_{\alpha}H$ region of CTX A3 at pH 6.0. Sequence-specific assignments of these heteronuclear correlation peaks are designated with the one-letter code for amino acids and residue number.

identified by the combination of NOESY and ROESY experiments (*7*, *40*).

In the case of CTX A3, only one cross-peak from Met26 could be attributed to protein-bound water. The NOEs and ROEs between CTX A3 NH protons and water protons are shown in Figure 6A. Only the NH of Met26 meets the criteria for the presence of tightly associated water (indicated by a dotted line) as suggested by Otting and Wuthrich (*26*). NOESY and ROESY cross-peaks at the water resonance may arise from three different magnetization transfer pathways as described previously (*12*, *13*). By comparison of the NOESY and ROESY spectra with the same mixing time of 75 ms at various temperatures (5, 27, and 45 °C), the three kinds of transfer pathways could be distinguished unambiguously. For positive NOESY and ROESY cross-peaks, it is necessary to consider the possibility of direct chemical exchange. Negative ROESY cross-peaks along with positive NOESY cross-peaks may be attributed to either exchange-relayed NOEs or protein-bound water NOEs. Only if the protein proton involved in the cross-peak is far from any highly exchange labile proton (at least 4−5 Å) can it be considered a candidate of protein-bound water NOEs and can the possibility of exchange-relayed NOEs be excluded. The remaining cross-peaks are presumably due to either direct fast exchange with water molecules or an indirect NOE effect caused by the neighboring protons undergoing fast exchange (labeled with asterisks). Since Tγ is known from X-ray crystallography to contain bound water, it is of interest to establish the validity of the NOE−ROE approach in detecting bound water in this class of biomolecules. Comparison of the 2D ROESY spectra for CTX A3 and Tγ demonstrated that Tγ exhibited a similar water−Met26 cross-peak as shown in Figure 6B. Therefore, the location of the bound water as identified by NMR was essentially the same as that in the structure of Tγ derived from X-ray diffraction.

Once the putative water location was established, the relative coordinates of the bound water and neighbor residues were constructed and the resulting structures were refined to give the lowest-energy structure shown in the top panel of Figure 2B. The relative position of the atoms (painted by balls) involved in the formation of hydrogen bonds with a bound water molecule within the water binding loop and the correspondent structural and sequence comparisons of five different P-type CTXs are depicted in the lower panel of Figure 2B. The atoms share similar coordinates, and the overall loop structures superimpose well. It appears that the two Pro amino acid residues near this region play an important role in the formation of the water binding loop since they are the only two conserved amino acid residues within the loop. However, if we exclude CTX A5 from the comparison (because CTX A5 has a slightly different structure in this region with one additional residue), a consensus sequence, MxAxPxVPV, might be derived for this region.

To gain further insight into the potential nature of the structure and dynamics of the bound water, a molecular dynamics simulation of the CTX A3 molecule with a bound water molecule soaked with a 5 Å water layer (603 water molecules) was performed. As indicated by the black stripe shown in Figure 7, the bound water molecule can form a stable hydrogen bond not only with the NH of Met26 (Figure 7A) but also with the CO of Thr29 (Figure 7B) and/or Val32 (Figure 7C) during the simulation time (500 ps). Internal 180° flips around the axis of the water−NH bond can also be seen to occur during this time period, as indicated by arrows in Figure 7. Other surface water molecules appear to diffuse freely with short mean residence times, shorter than 50 ps. This is apparent in Figure 7D, where the mobility of five randomly chosen surface water molecules with similar initial distances (10 Å) to the NH of Met26 is shown. The

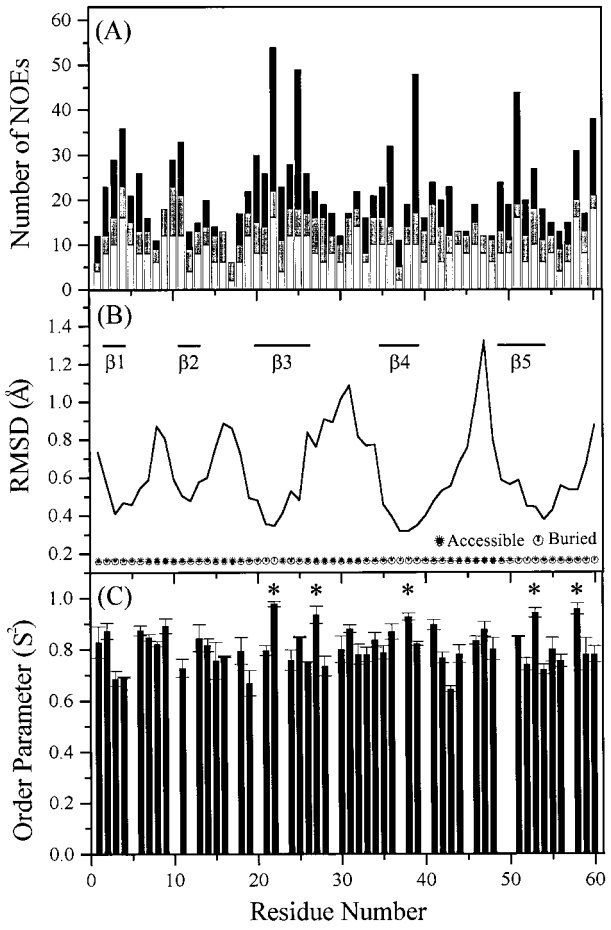

FIGURE 5: Structural dynamics of CTX A3 as a function of amino acid residue position as indicated by the (A) distribution of long-range (black), medium-range (dark gray), sequential (light gray), and intraresidual (white) NOE distance constraints. (B) Root-mean-square deviations (rmsds) of backbone atoms for 20 calculated protein structures and (C) order parameter (S^2) values (average of 400 and 600 MHz) for the backbone $C_\alpha H$.

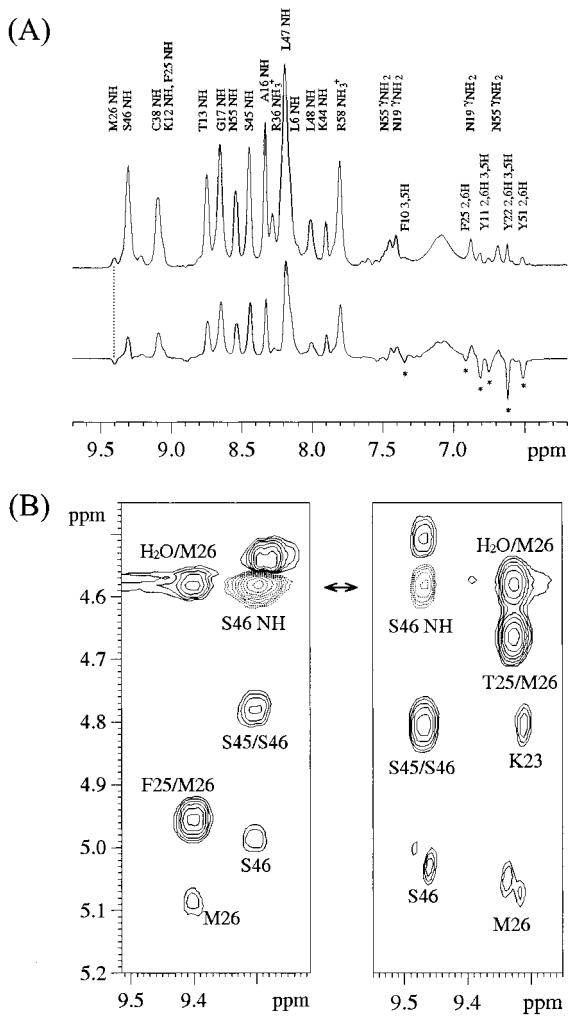

FIGURE 6: (A) Cross sections taken at the ω_1 chemical shift of the water resonance through the 2D spectra recorded in the laboratory frame (NOESY) (top) and the rotating frame (ROESY) (bottom) for CTX A3 at 45 °C. The cross-peaks aligned along the water resonance are identified and labeled above the figure. The dashed line and the asterisks indicate the existence of bound water and the exchange-related NOEs, respectively. (B) Contour plots for the ROESY spectra for CTX A3 (left) and Tγ (right), depicting the interaction of the M26 amide proton with bound water. The arrows denote the ω_1 chemical shift of the water resonance.

results of the MD are consistent with a bound water molecule which has a residence time of >500 ps.

To exclude the possibility that the simulations may be biased by the starting point of each simulation, the CTX A3 structure without a bound water molecule within the loop was soaked with a 5 Å water layer. Figure 7E shows that surface water molecules can penetrate quickly into the interior of the loop II region. The penetration process took less than 10 ps for four of five independent calculations using different initial water coordinates. In addition, after diffusing into the water binding loop, the water molecule forms a stable hydrogen bond network with a long residence time as shown before. In contrast, there are other surface water molecules that initially form hydrogen bonds with the NH and/or CO of amino acid residues near the region (e.g., with the CO of Leu48 and the NH of Val27 and Ala28), but they are found to diffuse away from the binding site within 50 ps. The simulation results provide further support for the reliability of the lifetime of the water bound to loop II.

It should be emphasized that the bound water and the nearby amino acid residues within the loop are highly accessible to the solvent (Figures 2C and 5B). Many hydrophobic amino acid residues (green color atoms) are surrounding the water binding site, and the Phe25 side chain even blocks partially the water pathway on one side of the molecule (top panel in Figure 2C). However, the molecular dynamics simulation indicated that a slight tilting of the Phe25 side chain allows the formation of a water pathway by forming a hydrogen bond between the bound water and surface water molecules. In fact, the residence time for those water molecules hydrogen bonded to the bound water may range from 15 to 200 ps.

The trajectory for the surface water molecule in becoming loop II-bound water provides interesting information about understanding the role of the consensus sequence, MxAx-PxVPV, in forming the water binding loop. In all five molecular dynamics simulations shown in Figure 7E, penetration of water into the loop can only occur through the convex side of the loop (bottom panel in Figure 2C) with initial hydrogen bond formation with the CO of Val32. Apparently, after hydrogen bonding with the CO of Val32, the water molecule tends to remain there for less than 5 ps, followed by the final hydrogen bond formation with the NH of Met26 and the CO of Thr29. During this short time period,

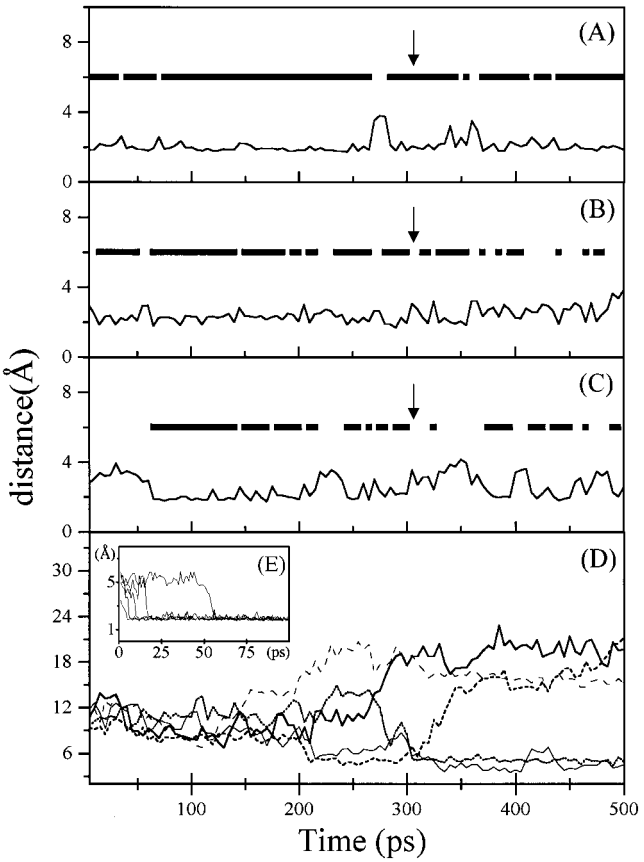

FIGURE 7: Molecular dynamics simulation of the mobility of the bound water molecule as indicated by the distance between (A) the H_2O oxygen and the Met26 NH proton, (B) the H_2O hydrogen and the Thr29 CO oxygen, and (C) the other H_2O hydrogen and the Val32 CO oxygen during the 500 ps simulation time. The black bars in each panels recorded the existence of hydrogen bonds and the arrows indicated the bound water molecule undergoing a 180° flip (see the text). (D) The distances between the Met26 NH proton and the oxygen atom for five randomly chosen water molecules are also traced to monitor the mobility of surface waters. (E) Penetration of the water molecule from the surrounding water layer into the interior of the water binding loop to become a tightly bound water molecule. The distance between the water oxygen and the Met26 NH was traced by sampling the trajectory at 1 ps intervals with a total simulation period of 100 ps.

the CO of Pro33 may serve as another hydrogen bond acceptor to keep the bound water remaining in the loop. Therefore, Met26, Val32, and Pro33 appear to provide an environment suitable for the penetration of a water molecule within a relatively hydrophobic environment.

The quantitative determination of the cross-relaxation rates is difficult for the weak NOE between the bound water molecule and the NH of Met26, although the ratio of the signal intensity between NOESY and ROESY (Figure 6A) can, in principle, be used to characterize the residence times of the bound water on CTX A3 (*22*). Characterization of the dynamics of bound water via the NOE−ROE method will become insensitive especially when the residence time is longer than nanoseconds. To develop a clearer understanding of the role of the bound water, it is essential to establish that the NOESY and ROESY cross-peak does not simply reflect the interim visit of bound water to the cavity formed by the water binding loop.

^{17}O NMR and Bound Water Dynamics. While the NOE−ROE results and MD simulations are consistent with the presence of a water molecule that is bound to CTX A3 with a lifetime of >500 ps, support for the conclusion is desirable since this water molecule is accessible to solvent and is not buried in a cavity. Recent studies have demonstrated that triple-quantum filtered (3QF) NMR of $H_2{}^{17}O$ (*18*−*22*) in the presence of biological macromolecules may be used to investigate the lifetime and the total number of bound water molecules. Figure 8 shows the dependence of the ^{17}O NMR signal amplitude as a function of the evolution time t_1 of the 3QF transverse relaxation experiment. To determine the number of water molecules that are bound to CTX A3, the amplitudes of the 3QF spectra were fit directly as a function of the evolution period. The results are given in Table 2, and a typical fit between experimental and calculated data is shown in Figure 8. Note that the calculated profile decays more rapidly than the experimental profile. It is reasonable to suggest that this behavior arises from the presence of the non-3Q signal that is not canceled by the phase cycling that is used since a sample of D_2O alone gave for the same t_1 values a residual signal when $t_1 < T_2$ ($D_2{}^{17}O$). The amplitudes of the 3QF spectra in Figure 8 were then corrected for the non-3Q signal by measuring the signal amplitudes for a D_2O (20 atom % O^{17}) sample under experimental conditions identical to those used for the CTX A3 sample and subtracting the D_2O amplitudes from those in Figure 8 at the corresponding t_1 value. The t_1 dependence of the resulting "corrected" amplitudes was fit with S^2 values of 1.0 and 0.7. The best-fit results gave values for p_b and τ_c that were very

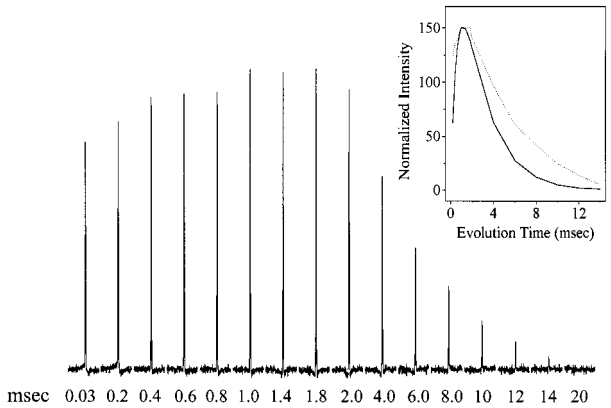

FIGURE 8: Dependence of the ^{17}O 3QF signal amplitude on evolution time t_1 (milliseconds). The comparison of the experimental (···) and calculated (—) amplitudes of the ^{17}O 3QF transverse signal as a function of the evolution time t_1 is inserted in the upper-right corner. The calculated profile represents the best fit of the experimental data with a p_b of 6×10^{-4} (one bound water molecule per CTX A3), a τ_c of 6 ns, and a T_2 of 3 ms for bulk water.

Table 2: ^{17}O Correlation Times and Bound Fraction for Water Associated with CTX A3[a]

	τ_c (ns)	p_b	no. of water molecules/toxin
$I(t_1)$[b]	4.98 ± 0.06	0.00070 ± 0.00006	1.30 ± 0.12
$I(t_1) - I_{D_2O}(t_1)$	5.25 ± 0.22	0.00063 ± 0.00003	1.20 ± 0.06
$I(t_1) - I_{D_2O}(t_1)$ ($S^2 = 0.7$)	7.02 ± 0.01	0.00084 ± 0.00004	1.60 ± 0.07
FID	5.85 ± 0.16	0.00039 ± 0.00001	0.74 ± 0.02
FID ($S^2 = 0.7$)	5.95 ± 0.20	0.00055 ± 0.00001	1.06 ± 0.02

[a] Averages are calculated from the best-fit results of 30 data sets in which the amplitudes were varied randomly within the range of the estimated signal-to-noise error. [b] The data without mention of the order parameter (S^2) were fitted with an S^2 of 1.

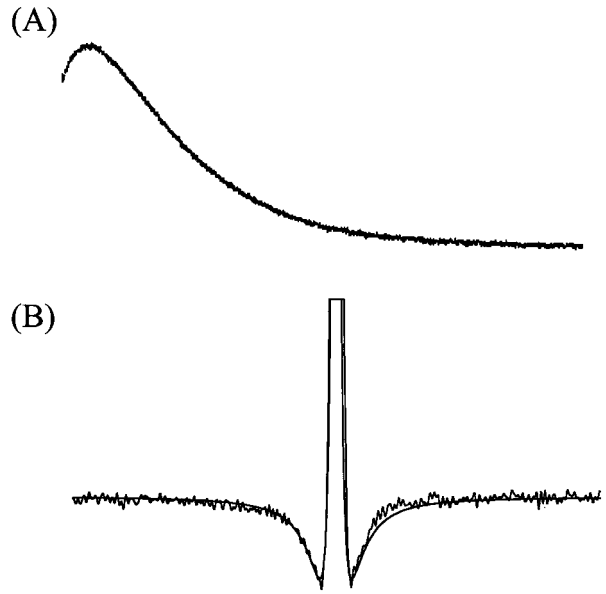

FIGURE 9: ^{17}O NMR FID (A) and corresponding spectrum (B) of CTX A3 at 22 °C. The calculated spectrum (—) representing the best fit of the experimental data with an evolution time t_1 of 1.4 ms, a p_b of 3.9×10^{-4}, a τ_c of 5.85 ns, an S^2 of 1.0, and a T_2 (for bulk water) of 3 ms is shown with the experimental spectrum.

similar to those obtained by fitting the raw data (Table 2), while correlation times were found to be 5.25 and 7.02 ns, respectively. CTX A3 at 5 mM in aqueous buffer has an overall correlation time of 3.8−4.5 ns at 25 °C (by ^{13}C relaxation measurement). Thus, it may be expected that the viscosity of a 28 mM solution of the toxin is somewhat greater, leading to the longer correlation times required to fit the 3QF transverse relaxation data. It should be emphasized that in fitting both of these data sets, fits with comparable errors were obtained in some cases where the correlation time is on the order of 20 ns and the associated fraction of bound water was less than 0.25 H_2O per CTX A3. In such cases, the results are not physically plausible since from ^{13}C NMR relaxation studies the correlation time of CTX A3 is <10 ns, so we can simply rule out this possibility. Such cases additionally reflect another fact that the value of $\mathbf{R}_{bulk}$ depends on the product p_b and τ_c.

^{13}C relaxation studies indicated that internal motions of limited amplitude existed in the water binding region characterized by an order parameter, S^2, with an average value of 0.7 (Figure 5C). Allowing for such motion in the analysis of the 3QF transverse relaxation data did not significantly improve the fitting procedure (Table 2).

In addition to fitting the dependence of the 3QF signal amplitude on the evolution time t_1, an alternate approach is to fit either the free induction decay (FID) or the spectral line shape acquired at a value of t_1, which gives the maximal signal intensity. A spectrum (Figure 9) was acquired with a t_1 value of 1.4 ms and with a 10-fold increase in the signal-to-noise ratio relative to that of the spectra depicted in Figure 8. A fit of the calculated FID to the experimental FID is shown in Figure 9A, and the parameters that give the best fit are given in Table 2. The experimental FID decays more slowly than the calculated one. This is similar to the results depicted in Figure 8, suggesting the presence of an additional signal that does not arise from the 3Q filter. Inspection of the spectral line shape in Figure 9B shows negative "dips" characteristic of the triexponential line shape of ^{17}O undergoing motion in the nonextreme narrowing regime. The spectral line shape showed clear evidence of a water molecule, which is indeed immobilized by the toxin. The predicted spectrum in Figure 9B reproduced the negative features of the line shape, although the central intensity was less than the experimental intensity. This effect can be attributed to incomplete cancellation of a single-quantum signal that is superposed on that of the desired signal. However, even with this limitation, the values of τ_c and p_b are comparable to those obtained by analysis of data obtained by varying the evolution time t_1.

The 3QF transverse relaxation data are consistent with the fraction of water molecules bound to the toxin having a value ranging from 3.9×10^{-4} to 8.4×10^{-4}(Table 2). For a 28 mM solution of CTX A3, the fraction of bound water that corresponds to one water molecule bound per toxin is calculated to be 5.2×10^{-4}. The values obtained from ^{17}O NMR are consistent with one water molecule bound per toxin. The results presented here are also consistent with a model in which the bound water molecule does not undergo additional fast motion of a large amplitude within the binding region.

In the fitting of the data, the ^{17}O quadrupolar coupling constants for free and bound water were assumed to be equal with values of 7.6 MHz. Similar values have also been adopted by previous studies of protein-bound water (*21*). Since a recent study has suggested that the quadrupolar coupling constant of water may have a value of 6.5 MHz (*22*), it is desirable to estimate the possible error that might arise from the variation of ^{17}O quadrupolar coupling constants used for analysis. The effect on these results of replacing the quadrupolar coupling constant value of 7.6 MHz with a value of 6.5 MHz in the fitting of that data would be to scale the product $\tau_c p_b$ by $(7.6/6.5)^2$ or 1.36. Inspection of Table 2 indicates that the correlation time would be increased to ∼7−8 ns for one water molecule per CTX A3. An actual fit of the data in Figure 8 gave a τ_c of 6.4 ns and 1.45 waters per CTX. Thus, the conclusion that the results are consistent with one bound water molecule is not affected by the choice of possible values for the ^{17}O quadrupolar coupling constant.

While it is not possible with these data to delineate the details of the local motion of the water molecule within the binding region of CTX A3, it is possible to draw some general conclusions about the time scale of the water toxin association. The data demonstrate that the motion of the water molecule approaches that of the overall motion of the protein. Thus, the residence time of the bound water molecule must be greater than the correlation time of the toxin (∼5−7 ns). The upper limit of the residence time would be defined by the T_2 of ^{17}O of the bound water. With a correlation time of 5−7 ns, the T_2 is expected to be on the order of 100 μs. On the basis of these considerations, the range of the residence time for the bound water molecule on CTX A3 is estimated to be 5 ns to 100 μs.

Role of Bound Water. In this study, we have demonstrated the proximity of a single bound water molecule with long residence time (>5 ns) in a solvent accessible, structurally flexible, and functionally important loop of P-type CTXs. Since all the P-type CTXs adopt a three-fingered structure with four disulfide bonds in the core region, it is tempting to hypothesize that such a bound water in the membrane

binding loop may modulate the membrane binding activities of the amphiphilic P-type CTXs, speculation that is attractive when one notes their structural similarity in the water binding loop.

One may rationalize how water may modulate the membrane binding activities of the amphiphilic P-type CTXs as follows. First, the exchange of bound water near the hydrophobic tip of loop II may regulate the toxin's structural stability, leading to the formation of the extended hydrophobic domain of the P-type CTXs. The water helps to maintain the spatial ω shape of loop II by forming a stable hydrogen bond network with the protein backbone. As a result, loop II is extended to make contact with loop I and loop III to form a continuous hydrophobic patch. This hydrophobic patch has been proven to be the membrane binding region (*7*, *9*). If the exchange rate of the bound water is reduced on binding to phospholipid membranes to favor patch formation, then it is readily seen how the dynamics of bound water can become an important regulating factor for the membrane association of P-type CTXs. It is reasonable to expect that bulk water will be excluded from the surface region where the toxin and membrane are in close contact. As a result, the exchange rate of bound water is reduced with a concomitant stabilization of the toxin's hydrophobic patch, possibly through the strengthening of the hydrogen bond in the tip of the loop. Such an effect of membrane surface binding on the water exchange rate may be speculative, but it is reasonable. Studies on membrane−protein binding have demonstrated that hydrogen exchange rates can be significantly slowed in those regions of the sequence that are in the proximity of the membrane surface (*50*−*52*). In this case, it would be difficult to study the dynamics of bound water in the CTX−phospholipid micellar complex by 3QF ^{17}O NMR, since there are several water molecules that are tightly associated with phospholipid headgroups (*53*). However, in the case of toxin CTII, binding to DPC micelles leads to a shift of the Met26 NH proton resonance by 0.8 ppm relative to that of the free state (*7*). As a result, it was possible to monitor the exchange broadening of the Met26 NH resonance upon micellar binding, from which it was determined that amide exchange of the loop II of CTII is slowed to a time scale of a few milliseconds (*7*). In fact, by monitoring the intermolecular NOE between CTX A3 and lysophosphatidylcholine, we found phospholipid molecules to bind to the convex side of the CTX A3 molecule (data not shown). In addition, the intensity of the NOE between the bound water molecule and the NH of Met26 also increases by 3-fold under conditions where binding of CTX A3 to lysophosphatidylcholine micelles is saturated. Therefore, the structure and dynamics of the water binding loop are likely to be significantly perturbed upon binding to phospholipid membranes.

A second way in which water may modulate the membrane binding activities of the amphiphilic P-type CTXs is by influencing the equilibrium between the bound forms of the toxin. Depending on whether the hydrophobic thickness of the lipid bilayer can match the continuous hydrophobic patch formed by the three loops of the P-type CTX, the toxin can bind reversibly to a phospholipid membrane in either the peripheral or penetrating mode. If the bound water molecule can help to extend the conformation of loop II as suggested, the existence of bound water will indeed change the hydrophobic distribution formed by the loops and influence the matching to the hydrophobic domain of the membrane. As a result, the exchange rate of the bound water can further modulate the population of the two peripheral and penetrating membrane binding modes.

Finally, it is intriguing to see the relatively long residence time of the loop II-bound water despite the solvent accessibility and dynamic nature of this loop. However, it has been pointed out before that for a water molecule in a surface pocket, the residence time should be determined by the activation energy needed for the water molecule to pass through the least hydrogen-bonded state on its way out of the pocket (*16*). The number of water−peptide hydrogen bonds is not the major determining factor for long residence times, since, as we demonstrated in computer simulation, other surface water molecules with short residence times are also extensively hydrogen bonded. It will be interesting in the future to study how the the consensus sequence depicted here provides an environment sufficient for a long residence time of the bound water.

CONCLUSION

Dynamic characterization of the water binding loop in the P-type cardiotoxin has been carried out using ^{1}H and ^{13}C NMR techniques to better understand its structure−function relationship. Specifically, it has been demonstrated by using ^{1}H and ^{17}O NMR techniques that there is a single long-lived bound water molecule located within the solvent accessible loop of P-type CTX A3. The residence time is in the range of 5 ns to 100 μs. Analysis of the ^{13}C relaxation data of the polypeptide backbone further indicates that the water binding loop is more flexible than the core regions of the toxin. For five known 3D structures of P-type CTXs determined by NMR and/or X-ray methods, the region of the toxin in which bound water molecules have been located appears to be structurally conserved. These results combined with those of others studies suggest that there is a consensus sequence for the water binding loop and that there is an important structural role of two proline residues for its formation. Since the water binding loop is also involved in its binding to phospholipid membranes, the role of bound water could be to regulate the membrane binding mode required for the general cytotoxic effect of amphiphilic P-type CTXs.

REFERENCES

1. Dufton, M. J., and Hider, R. C. (1988) *Pharmacol. Ther. 36*, 1−40.
2. Dufton, M. J., and Hider, R. C. (1991) in *Snake Venom* (Harvey, A. L., Ed.) pp 259−272, Pergamon Press, New York.
3. Chien, K.-Y., Chiang, C.-M., Hseu, Y.-C., Vyas, A. A., Rule, G. S., and Wu, W. (1994) *J. Biol. Chem. 269*, 14473−14483.
4. Chien, K.-Y., Huang, W.-N., Jean, J.-H., and Wu, W. (1991) *J. Biol. Chem. 266*, 3252−3259.
5. Sue, S.-C., Rajan, P. K., Chen, T.-S., Hsieh, C.-H., and Wu, W. (1997) *Biochemistry 36*, 9826−9836.
6. Wu, W. (1997) *J. Toxicol. 16*, 115−134.
7. Dubovskii, P. V., Dementieva, D. V., Bocharov, E. V., Utkin, Y. N., and Arseniev, A. S. (2001) *J. Mol. Biol. 305*, 137−149.
8. Sun, Y.-J., Wu, W., Chiang, C.-M., Hsin, A.-Y., and Hsiao, C.-D. (1997) *Biochemistry 36*, 2403−2413.
9. Dauplais, M., Neumann, J. M., Pinkasfeld, S., Menez, A., and Roumestand, C. (1995) *Eur. J. Biochem. 230*, 213−220.

10. Bilwes, A., Rees, B., Moras, D., Menez, R., and Monez, A. (1994) *J. Mol. Biol. 239*, 122−136.
11. Rose, G. D., Young, W. B., and Gierasch, L. M. (1983) *Nature 304*, 654−656.
12. Otting, G., and Liepinsh, E. (1995) *Acc. Chem. Res. 28*, 171−177.
13. Otting, G. (1997) *Prog. NMR Spectrosc. 31*, 259−285.
14. Kay, L. E., Nicholson, L. K., Delaglio, F., Bax, A., and Torchia, D. A. (1992) *J. Magn. Reson. 97*, 359−375.
15. Farrow, N. A., Muhandiram, R., Singer, A. U., Pascal, S. M., Kay, C. M., Gish, G., Shoelson, S. E., Pawson, T., Forman-Kay, J. D., and Kay, L. E. (1994) *Biochemistry 33*, 5984−6003.
16. Denisov, V. P., and Halle, B. (1995) *J. Mol. Biol. 245*, 682−697.
17. Weisner, S., Kurian, E., Prendergast, F. G., and Halle, B. (1999) *J. Mol. Biol. 286*, 233−246.
18. Baguet, E., and Hennebert, N. (1999) *Biophys. Chem. 77*, 111−121.
19. Torres, A. M., Grieve, S. M., and Kuchel, P. W. (1998) *Biophys. Chem. 70*, 231−239.
20. Torres, A. M., Grieve, S. M., Chapman, B. E., and Kuchel, P. W. (1997) *Biophys. Chem. 67*, 187−198.
21. Baguet, E., Chapman, B. E., Torres, A. M., and Kuchel, P. W. (1996) *J. Magn. Reson., Ser. B 111*, 1−8.
22. Lehoux, A., Krystyniak, M., and Baguet, E. (2001) *J. Magn. Reson. 148*, 11−22.
23. Chung, C.-W., and Wimperis, S. (1992) *Mol. Phys. 76*, 47−81.
24. Jaccard, G., Wimperis, S., and Bodenhausen, G. (1986) *J. Chem. Phys. 85*, 6282−6293.
25. Denisov, V. P., Halle, B., Peters, J., and Horlein, H. D. (1995) *Biochemistry 34*, 9046−9051.
26. Otting, G., Liepinsh, E., and Wuthrich, K. (1991) *Science 254*, 974−980.
27. Rance, M., Sorensen, O. W., Bodenhausen, G., Wagner, G., Ernst, R. R., and Wuthrich, K. (1983) *Biochem. Biophys. Res. Commun. 117*, 479−485.
28. Bax, A., and Davis, D. G. (1985) *J. Magn. Reson. 65*, 355−360.
29. Piotto, M., Saudek, V., and Sklendar, V. (1992) *J. Biomol. NMR 2*, 661−665.
30. Nilges, M., Clore, G. M., and Gronenborn, A. M. (1988) *FEBS Lett. 239*, 129−136.
31. Williamson, M. P., and Asakura, T. (1993) *J. Magn. Reson., Ser. B 101*, 63−71.
32. Asakura, T., Taoka, K., Demura, M., and Williamson, M. P. (1995) *J. Biomol. NMR 6*, 227−236.
33. Szyperski, T., Wider, G., Bushweller, J. H., and Wuthrich, K. (1993) *J. Biomol. NMR 3*, 127−132.
34. Lipari, G., and Szabo, A. (1982) *J. Am. Chem. Soc. 104*, 4546−4559.
35. Wand, A. J., Urbauer, J. L., McEvoy, R. P., and Bieber, R. J. (1996) *Biochemistry 35*, 6116−6125.
36. Brisson, J. R., Uhrinova, S., Woods, R. J., van der Zwan, M., Jarrell, H. C., Paoletti, L. C., Kasper, D. L., and Jennings, H. J. (1997) *Biochemistry 36*, 3278−3292.
37. Press, W. H., Teukolsky, S., Vetterling, W. T., and Flannery, B. R. (1992) *Numerical Recipes in C*, Cambridge University Press, Cambridge, U.K.
38. Bhaskaran, R., Huang, C.-C., Chang, D.-K., and Yu, C. (1994) *J. Mol. Biol. 235*, 1291−1301.
39. Chiang, C.-M., Chang, S.-L., Lin, H.-J., and Wu, W. (1996) *Biochemistry 35*, 9177−9186.
40. Dementieva, D. V., Bocharov, E. V., and Arseniev, A. S. (1999) *Eur. J. Biochem. 263*, 152−162.
41. Bhaskaran, R., Huang, C.-C., Tsai, Y.-C., Jayaraman, G., Chang, D.-K., and Yu, C. (1994) *J. Biol. Chem. 269*, 23500−23508.
42. Bodenhausen, G., and Ruben, D. (1980) *Chem. Phys. Lett. 69*, 185−189.
43. Lo, C.-C., Hsu, J.-H., Sheu, Y.-C., Chiang, C.-M., Wu, W., Fann, W., and Tsao, P.-H. (1998) *Biophys. J. 75*, 2382−2388.
44. Richarz, R., Nagayama, K., and Wuthrith, K. (1980) *Biochemistry 19*, 5189−5196.
45. Loosli, H. R., Kessler, H., Oschkinat, H., Weber, H. P., Petcher, T., and Widmer, A. (1985) *Helv. Chim. Acta 68*, 682−693.
46. Nirmala, N. R., and Wagner, G. (1988) *J. Am. Chem. Soc. 110*, 7557−7559.
47. Lee, C.-S., Kumar, T. K. S., Lian, L.-Y., Cheng, J.-W., and Yu, C. (1998) *Biochemistry 37*, 155−164.
48. Guenneugues, M., Drevet, P., Pinkasfeld, S., Gilquin, B., Menez, A., and Zinn-Justin, S. (1997) *Biochemistry 36*, 16097−16108.
49. O'Connell, J. F., Bougis, P. E., and Wuthrich, K. (1993) *Eur. J. Biochem. 213*, 891−900.
50. Heimburg, T., and Marsh, D. (1993) *Biophys. J. 65*, 2408−2417.
51. Keire, D. A., and Kobayashi, M. (1998) *Protein Sci. 7*, 2438−2450.
52. McGuire, A. M., Matsuo, H., and Wagner, G. (1998) *J. Biomol. NMR 12*, 73−88.
53. Hsieh, C.-H., and Wu, W. (1996) *Biophys. J. 71*, 3278−3287.

BI010848F